*inorganics*

MDPI

*Article*

# In Situ Studies and Magnetic Properties of the *Cmcm* Polymorph of $LiCoPO_4$ with a Hierarchical Dumbbell-Like Morphology Synthesized by Easy Single-Step Polyol Synthesis

**Carlos Alarcón-Suesca [1,†], Jennifer Ludwig [1,†], Viktor Hlukhyy [2], Christoph Stinner [3] and Tom Nilges [1,*]**

1 Synthesis and Characterization of Innovative Materials, Department of Chemistry, Technical University of Munich, Lichtenbergstraße 4, 85747 Garching, Germany; carlos.alarcon@tum.de (C.A-S.); jennifer.ludwig@tum.de (J.L.)

2 Chair of Inorganic Chemistry with Focus on Novel Materials, Department of Chemistry, Technical University of Munich, Lichtenbergstraße 4, 85747 Garching, Germany; viktor.hlukhyy@tum.de

3 BMW AG, Petuelring 130, 80788 München, Germany; christoph.stinner@bmw.de

* Correspondence: tom.nilges@lrz.tum.de; Tel.: +49-89-289-13111

† These authors contributed equally to this work.

Academic Editor: Richard Dronskowski

Received: 6 October 2016; Accepted: 10 November 2016; Published: 17 November 2016

**Abstract:** $LiCoPO_4$ (LCP) exists in three different structural modifications: LCP-*Pnma* (olivine structure), LCP-$Pn2_1a$ ($KNiPO_4$ structure type), and LCP-*Cmcm* ($Na_2CrO_4$ structure type). The synthesis of the LCP-C*mcm* polymorph has been reported via high pressure/temperature solid-state methods and by microwave-assisted solvothermal synthesis. Phase transitions from both LCP-$Pn2_1a$ and LCP-C*mcm* to LCP-*Pnma* upon heating indicates a metastable behavior. However, a precise study of the structural changes during the heating process and the magnetic properties of LCP-C*mcm* are hitherto unknown. Herein, we present the synthesis and characterization of LCP-*Cmcm* via a rapid and facile soft-chemistry approach using two different kinetically controlled pathways, solvothermal and polyol syntheses, both of which only require relatively low temperatures (~200 °C). Additionally, by polyol, method a dumbbell-like morphology is obtained without the use of any additional surfactant or template. A temperature-dependent in situ powder XRD shows a transition from LCP-C*mcm* at room temperature to LCP-*Pnma* and finally to LCP-$Pn2_1a$ at 575 and 725 °C, respectively. In addition to that, the determination of the magnetic susceptibility as a function of temperature indicates a long-range antiferromagnetic order below $T_N$ = 11 K at 10 kOe and 9.1 K at 25 kOe. The magnetization curves suggests the presence of a metamagnetic transition.

**Keywords:** polymorph; $LiCoPO_4$-*Cmcm*; metamagnetic transition; in situ XRD; polyol; solvothermal; transition phase; hierarchical morphology

## 1. Introduction

Since their introduction by Whittingham [1] and commercialization in the early 1990s by Sony® [2], Li-ion batteries (LIB) have become a breakthrough technology in portable electronics. So far, LIB constituted the most appropriate method of energy storage in this sector because they show high energy density, low weight, design flexibility and long lifetime [3]. In current LIB technology, the electrochemical performance (e.g., cell voltage, capacity, $Li^+$ transportation rate) is mainly determined by the cathode material and, thus, intense research efforts are undertaken in this field [4]. Among several cathode materials, such as spinel types and lithium-rich layered oxides, lithium transition-metal

orthophosphates with the sum formula Li*M*$PO_4$ (*M* = Fe, Mn, Co, Ni) or simply L*M*P (LFP, LMP, LCP, LNP) have received particular attention due to their excellent electrochemical properties, good thermal stability, low cost and environmental friendliness [5]. While LFP and LMP have been widely investigated to date, LCP is still under investigation. In LCP, the $Co^{2+}/Co^{3+}$ redox couple offers a high operating voltage of approximately 4.8 V versus $Li/Li^+$ [6]. Moreover, LCP shows a high theoretical energy density of 800 Wh/kg (superior compared to the 580 Wh/kg of LFP), exhibits the lowest hole polaron migration barrier of the phospho-olivine family and subsequently has the highest electronic conductivity compared to LFP, LMP and LNP [7]. Furthermore, LCP shows a reduced cobalt weight fraction per formula unit compared to commercial $LiCoO_2$, making it a lower-cost option [8,9]. LCP can exist in three polymorphs with orthorhombic crystal structures, and several electrochemical and physical properties have been reported so far [10–12]. The most widely investigated one is olivine-type LCP-*Pnma*. In the structure, $Li^+$ and $Co^{2+}$ ions occupy octahedral sites and $P^{+5}$ is located in a tetrahedral environment formed by a distorted hexagonal close-packed (*hcp*) array of oxygen atoms [13]. The [$CoO_6$] octahedra form zigzag chains that are running parallel to the crystallographic *c* axis (Figure 1a). The chains are linked by the [$PO_4$] tetrahedra, resulting in a 3D network structure [14]. The $Li^+$ ions are located in channels along [010] and [001]. However, studies for olivine structures show that $Li^+$ diffusion is only promoted along the *b* direction due to a lower activation energy [15–17]. The second polymorph (Figure 1b) is LCP-$Pn2_1a$. This modification was theoretically predicted by Hautier [6] based on ab initio DFT calculations and subsequently experimentally reported by Jaehne et al. [18]. Unlike the olivine structure, $Co^{2+}$ cations are tetrahedrally coordinated in this structure. The framework features alternating corner-sharing [$PO_4$] and [$CoO_4$] tetrahedra along the *c* axis, the $Li^+$ diffusion paths are blocked by [$CoO_4$] tetrahedra and the compound shows a poor electrochemical performance. As a result, there are no direct $Li^+$ channels along any direction [6,18]. The third modification is LCP-*Cmcm*, which adapts the $Na_2CrO_4$-type structure (Figure 1c). This structure was first reported by Amador and co-workers[19] resulting from a high-pressure and high-temperature solid-state synthesis (6 GPa, 900 °C). In the structure, chains of edge-sharing [$CoO_6$] octahedra, which are running along the *c* direction, are cross-linked by [$PO_4$] tetrahedra along *a*. As a result, layers of the composition $[(CoO_6)(PO_4)]_\infty$ are generated. Moreover, the remaining tetrahedral sites are occupied by $Li^+$ ions and a high activation energy is required for $Li^+$-ion migration [19,20]. Recently, a microwave-assisted synthesis pathway was reported for LCP-C*mcm*. In this report, Manthiram et al. [21,22] claimed two conditions to be necessary for the formation of LCP-*Cmcm*: the use of fresh dried tetraethylene glycol (TTEG) as a solvent and the use of cobalt oxalate as a cobalt precursor. This synthesis was performed in a closed system using a temperature of 260 °C and a pressure below 30 bar. A transformation of LCP-*Cmcm* to LCP-*Pnma* revealed by thermal analysis was also reported in this study. Besides, an ex situ XRD analysis was conducted after a long annealing process (8 h) and posterior cooling of the material. However, there is no further information about the crystal structure at temperatures above 650 °C and/or further verification of any other possible transition during the cooling process. In addition, it is well known that morphology plays an important role in the electrochemical performance of cathode and anode materials for LIB [23–25]. Some reports explain the benefits of hierarchical dumbbell-shape morphologies such as larger surface area, high porosity and the formation of small-sized primary particles, leading to a reduction of the diffusion distance of lithium ions and an increase of reaction sites of $Li^+$-ions as well as preventing a decrease in volumetric energy density caused by low tap-density nanostructures [26,27]. Equally important, in order to achieve morphology control, the synthesis often requires the use of hydrothermal or solvothermal methods, sometimes microwave-assisted, as well as the use of expensive organic surfactants or additives, co-solvents and temperatures above 250 °C making the process expensive and complicated [28–30]. Herein, we report two alternative, kinetically controlled synthesis pathways towards the *Cmcm*-type LCP polymorph under mild conditions using a solvothermal as well as a polyol synthesis approach. Our synthesis is conducted at temperatures as low as 200 °C in a traditional round bottom flask. This simple synthesis does not require the use of water-free TTEG and is conducted using different cobalt ion precursors. The thermal behavior of LCP-*Cmcm* is examined comprehensively, revealing a

transformation of LCP-*Cmcm* to LCP-*Pnma* and finally to LCP-*Pn*$2_1$*a* at high temperature. Finally, the magnetic properties and metamagnetic transition of LCP-*Cmcm* are presented for the first time.

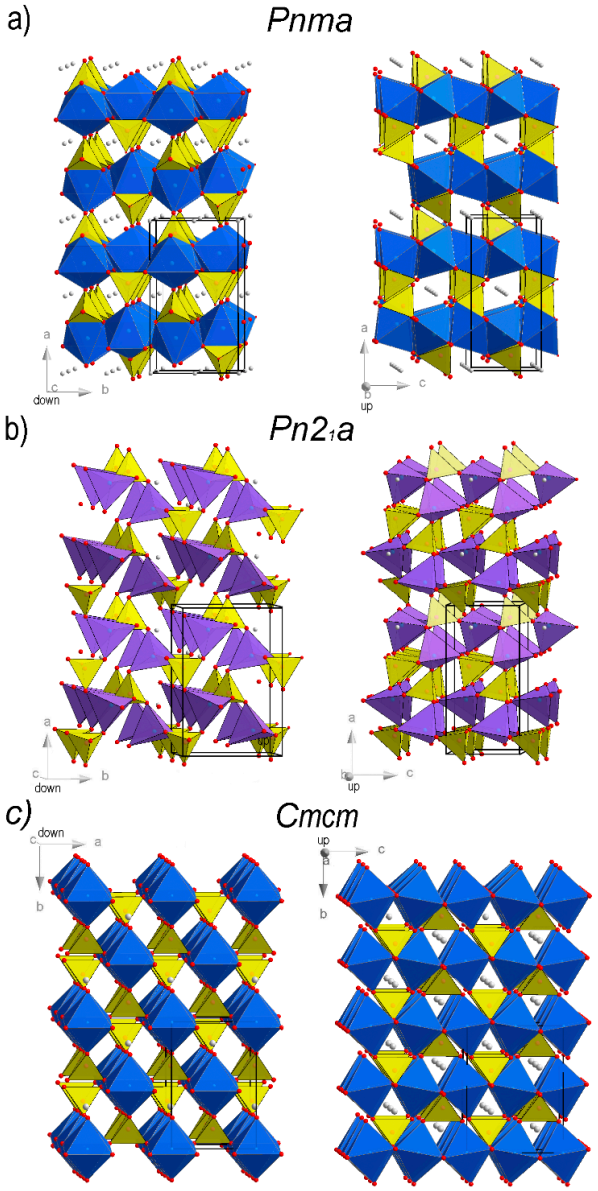


**Figure 1.** Projections of the crystal structures of the three orthorhombic polymorphs of $LiCoPO_4$ (LCP) along the crystallographic *c* and *b* axes with the space groups: (**a**) P*nma*; (**b**) P*n*$2_1$*a*; and (**c**) C*mcm*. [$CoO_6$] octahedra are drawn in blue, [$PO_4$] tetrahedra in yellow, [$CoO_4$] tetrahedra in purple, $Li^+$ ions in grey and $O^{2-}$ ions in red.

## 2. Results and Discussion

### *2.1. X-ray Powder Diffraction*

From solvothermal synthesis, the LCP polymorph with *Cmcm* symmetry was obtained from all solvents (see experimental section), yet varying amounts of $Li_3PO_4$ as well as traces of olivine-type LCP (space group *Pnma*) were observed as impurities (cf. Supplementary Materials, Figure S1, Tables S1–S3). The sample formed in diethylene glycol (DEG) solvent showed the smallest amount of impurities and was therefore selected for further characterization (designated as LCP-*Cmcm* (ST) in the following). Figure 2 shows the Rietveld refinement of the X-ray powder diffraction patterns

of the LCP-*Cmcm* samples obtained by solvothermal (ST) and polyol (PO) synthesis. The refined lattice parameters and refinement details are presented in Tables S2 and S3 of the Supplementary Materials. In the case of the solvothermal sample from the DEG solvent (Figure 2a), the refined lattice parameters are $a$ = 5.4347(4) Å, $b$ = 8.1638(5) Å, and $c$ = 6.2135(4) Å. However, very small amounts of $Li_3PO_4$, which is often formed in solution-based synthesis [31,32] and olivine-type LCP (space group *Pnma*) are observed as side phases. For the polyol sample (Figure 2b), no impurities were detected. All of the identified reflections can be fully indexed using the space group *Cmcm*. The refined lattice parameters $a$ = 5.4433(3) Å, $b$ = 8.1694(4) Å, and $c$ = 6.2129(3) Å are in good agreement with the values for LCP-*Cmcm* reported in the literature [19]. Atomic coordinates, thermal displacement parameters, and selected interatomic distances can be found in the Supplementary Materials (Tables S2–S4). Furthermore, the appearance of sharp diffraction peaks strongly reflects the high crystallinity of the samples produced at comparably low pressure, temperature and in a one-step synthesis without post-annealing. It has to be pointed out that, according to reference measurements presented in our previous work [33], the background can be fully attributed to the capillary and no amorphous components are present in the sample.

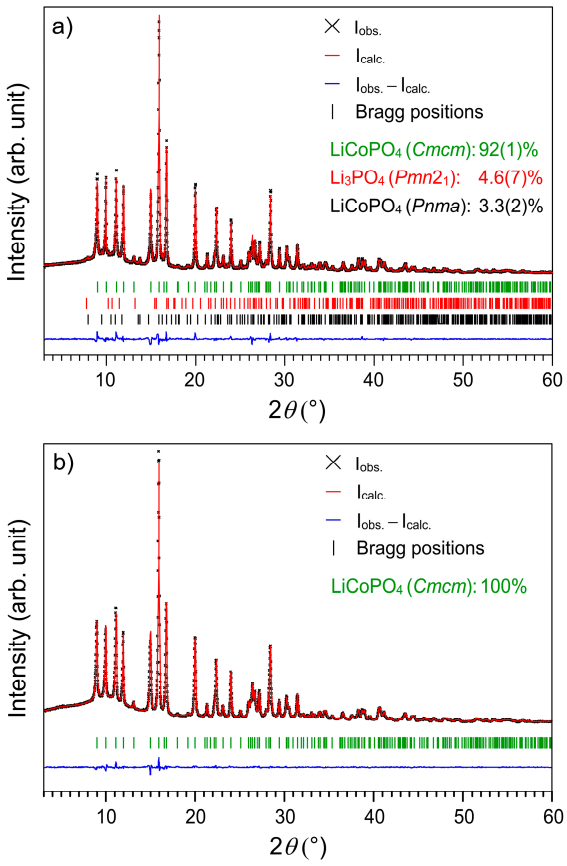


**Figure 2.** Rietveld fit of the X-ray powder diffraction data of LCP-*Cmcm* prepared by different synthesis pathways: (**a**) solvothermal; and (**b**) polyol synthesis.

### *2.2. Scanning Electron Microscopy (SEM)*

High-resolution SEM images (Figure 3) of the two materials reveal that the synthesis conditions strongly affect the morphology of the particles. The solvothermal synthesis results in the formation of irregular macrostructures formed by agglomeration of primary platelets with overall dimensions of 5–10 µm (Figure 3a,b). The agglomerates consist of cross-linked, leaf-shaped platelets of about 0.5–1 µm × 5–6 µm in size, and about 80 nm in thickness. Complex morphologies like this are generally obtained by solvothermal or hydrothermal routes [34]. On the contrary, the polyol synthesis

results in the formation of agglomerates with dumbbell or bow-tie shapes in the size range of 1–4 µm, which are formed by nanosheet-like primary particles with average dimensions of 20–40 nm in length, and 3–4 nm in thickness (Figure 3c,d). Given the fact that to date the synthesis of cathode materials with dumbbell-like morphologies is only reported by the use of templates and/or under solvothermal/hydrothermal conditions, and sometimes assisted by microwave irradiation [26,27,29], it is remarkable that such a well-organized hierarchical morphology was obtained by a simple synthesis approach. Moreover, this morphology type allows for the obtainment of materials with high surface areas which offer a larger interface between the electrode and the electrolyte, a fast intercalation probability and an improved electron transport as reported for LFP [30]. In our case, the polyol synthesis is conducted without the use of special additives or under high temperature or high pressure conditions. We suggest in accordance with the literature that the tetraethylene glycol acts not only as a solvent and mild reducing agent but also as a soft template to direct the growth and self-assembly of structures with preferred orientations [35]. Furthermore, the mixing order of the precursors has an influence on the morphology of the final product. Figure 3e,f show LCP particles prepared after direct mixing of the cobalt acetate and lithium acetate solutions and the subsequent addition of phosphoric acid. In this case, no primary nanosheet-like particles were observed but even primary nano-dots with the same bow-like morphology. This implies that only by a simple variation of the mixing sequence, the morphology can be modified, thereby inducing a change from primary nano-needles to primary nano-dots without the use of any surfactant or organic template. The crystal structure remains unaltered (not shown). Results of Fourier transform infrared spectroscopy (FT-IR), including band assignment and literature comparison, are presented in Figure S2 and Table S4 in the Supplementary Materials section.

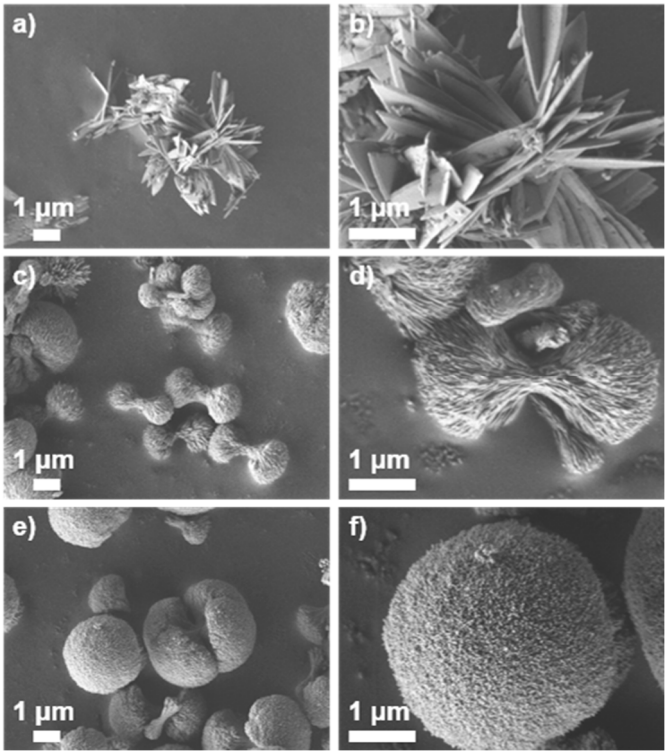


**Figure 3.** Scanning electron microscopy (SEM) images of LCP-*Cmcm* prepared by different procedures. (**a**,**b**) Solvothermal synthesis; (**c**,**d**) Polyol synthesis; Addition of $H_3PO_4$ to LiAc solution and posterior addition of $CoAc_2$ to $H_3PO_4$/LiAc mixture; (**e**,**f**) Polyol variation on the order of mixture: First mixture of $CoAc_2$ and LiAc with posterior addition of $H_3PO_4$ to the $CoAc_2$/LiAc mixture.

### 2.3. Elemental Analysis

The chemical composition of the samples was determined by means of CHNS (determination of the C, H, N, and S contents by combustion analysis) and AAS (atomic absorption spectroscopy) analyses. The results are given in Table 1. The Li:Co:P wt % ratio is found to be close to the theoretical composition 4.3:36.6:19.3 of $LiCoPO_4$ in both cases. The results correspond to Li:Co:P molar ratios of 0.99(5):0.97(3):1.00(2) and 0.93(5):0.91(5):1.00(2), implying that both materials are stoichiometric within three standard deviations. The CHNS analyses show that no significant amounts of hydrogen as well as carbon are present in the sample, which might be arising from residual water or the decomposition of residual organic polyol solvents and precursors. However, it has to be emphasized that, whereas the solvothermal sample tends to be stoichiometric, the phase pure polyol material seems to be deficient both in Li and Co. Hence, the results indicate that the synthesis method affects the stoichiometry of the phase. A more systematic investigation of the role of the synthesis route on the chemical composition will be the focus of oncoming research.

**Table 1.** Elemental analysis of LCP-*Cmcm* synthesized by (a) the solvothermal (ST) and (b) the polyol process (PO) [1,2].

| Element | (a) LCP(ST) | (b) LCP(PO) | Theoretical |
|---|---|---|---|
| C (wt %) | 0.7(3) | 0.8(3) | 0 |
| H (wt %) | 0.2(3) | 0.4(3) | 0 |
| Li (wt %) | 4.2(2) | 4.1(2) | 4.3 |
| Co (wt %) | 35(1) | 34(1) | 36.6 |
| P (wt %) | 18.9(3) | 19.6(3) | 19.3 |
| *n*(Li):*n*(P) | 0.99(5) | 0.93(5) | 1 |
| *n*(Co):*n*(P) | 0.97(3) | 0.91(3) | 1 |

[1] The composition is determined from the experimental values of the CHNS (combustion analysis to determine the C, H, N, and S contents) and AAS (atomic absorption spectroscopy) analyses (standard deviations in parentheses); [2] The N and S values were below the detection limit (= 0).

### 2.4. Thermal Stability and Phase Transformation

As reported previously, the polymorphs LCP-*Cmcm* and LCP-$Pn2_1a$ are metastable with transition temperatures to the thermodynamically stable LCP-*Pnma* of 220 and 550 °C, respectively [18,21,22]. However, all these conclusions were based on (a) TGA (thermogravimetric analysis)/DSC (differential scanning calorimetry) experiments which were only performed in a temperature range up to 700 and 500 °C, respectively, and (b) only supported by ex situ XRD analyses, which exclusively provide information about the particular phase at the end of the cooling process. Moreover, the reports were lacking additional SEM studies, which provide information about morphological changes upon heating. Taking the metastable behavior of LCP into consideration, it is important to examine the thermal behavior and respective phase transitions more thoroughly. The TGA/DSC data for the sample obtained by polyol synthesis are presented in Figure 4. In the TGA curve, a mass loss is observed between 200 and 300 °C, which can be attributed to the removal of residual water as well as to the decomposition of residues of the organic solvent. A strong signal occurs in the DSC experiment in the temperature range from 550 to 700 °C. At first glance, this effect can be attributed to the transition from LCP-*Cmcm* to LCP-*Pnma*, which represents a typical monotropic solid–solid phase transition of a metastable to a stable phase (irreversible process). Figure 5 shows the corresponding ex situ room temperature powder diffraction data of LCP-C*mcm* produced by the polyol method, in the temperature range between 200 and 900 °C with an increment of 100 °C and posterior cooling. Herein, the transformation of LCP-C*mcm* to LCP-*Pnma* takes place in the region between 500 and 700 °C. Moreover, the formation of an additional unidentified phase is evident. The corresponding peaks are marked with the symbol ♦.

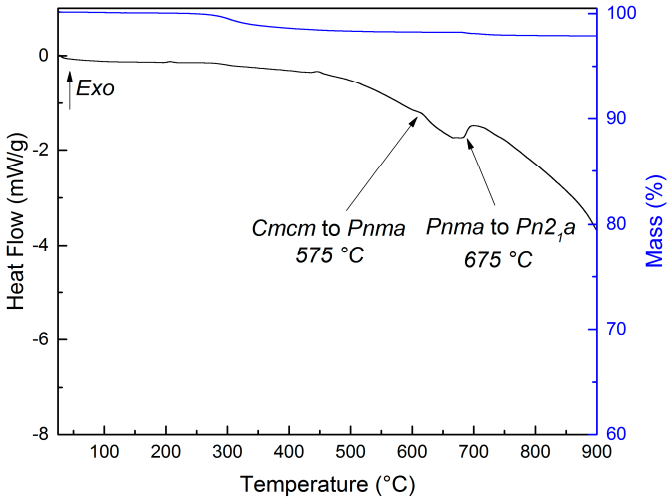


**Figure 4.** Thermal and gravimetric analyses for LCP-*Cmcm* (PO) obtained from the polyol route. TGA data are drawn in blue, and DSC data in black.

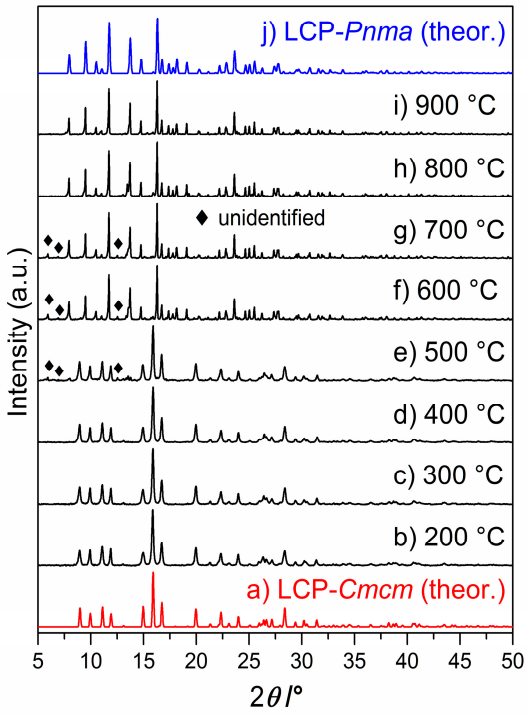


**Figure 5.** Ex situ X-ray powder diffraction patterns of LCP-*Cmcm* (PO) samples after heat treatment for 6 h in air in the temperature range from 200 to 900 °C (increment: 100 °C, **b**–**i**), in comparison with the theoretical patterns of LCP-*Cmcm* (**a**, **red**) and LCP-*Pnma* (**j**, **blue**). The quantitative transition from phase-pure LCP-*Cmcm* (**h**) to the olivine-type LCP-*Pnma* (**a**) can be observed upon heating. The reflections arising from an unidentified secondary phase are marked with the symbol ♦.

In order to elucidate the formation and stability of the phases at high temperatures without performing annealing and cooling steps in between, which is not suitable for the observation of metastable intermediates, we performed a temperature-dependent in situ powder XRD experiment between 21.8 and 600 °C. In Figure 6a, the section of the diffraction pattern is presented where the strongest reflections of LCP-*Cmcm*, (112) and (130), are observed. It can be clearly derived that the transformation to LCP-*Pnma* occurs at 575 °C. Hence, the data up to this temperature confirm the

metastable nature of LCP-*Cmcm*, which was reported previously [21]. To check the thermal stability, we further increased the temperature to 800 °C (Figure 6b). Surprisingly, the LCP-*Pnma* phase is only stable up to 625 °C, which is in strong contrast to any previous reports about the thermal behavior of olivine-type LCP [36,37]. The (101) and (210) peaks of LCP-*Pnma* are present from 575 to 625 °C. At 650 °C, no reflections are present in the measured range. Finally, starting from 675 °C, LCP-$Pn2_1a$ is formed, which is indicated by the characteristic (210) reflection. The two-phase transition temperatures found in the in situ XRD experiments are marked by two arrows in the DSC (differential scanning calorimetry) trace of Figure 4. After cooling from 800 °C to room temperature, the LCP-*Pnma* structure reemerges in the powder XRD (PXRD) pattern of the in situ study (see Figure S3). To the best of our knowledge, the complete thermal properties and phase stabilities touching all three LCP polymorphs are reported for the first time. Combining the information derived from in situ XRD and DSC experiments, it becomes obvious that the broad signal between 500 to 700 °C is caused by the phase transitions.

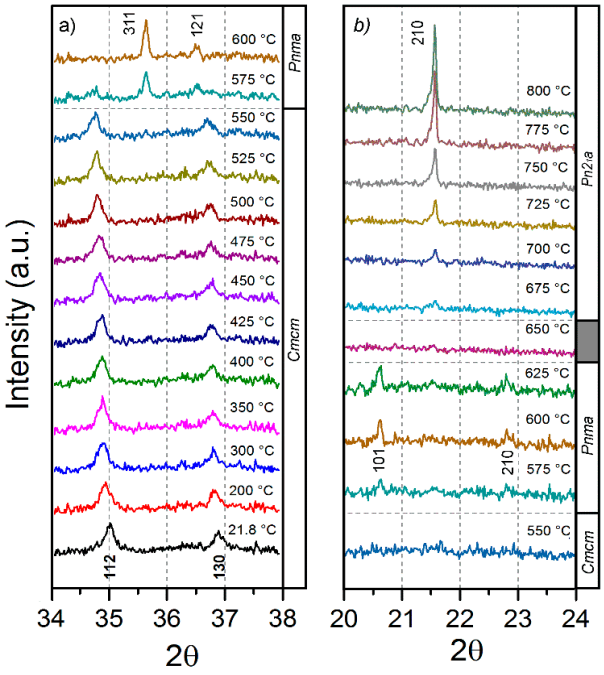


**Figure 6.** In situ X-ray powder diffraction patterns of LCP-*Cmcm* (PO): (**a**) Temperature range from 21.8 to 600 °C showing the transition from the *Cmcm* to the *Pnma* polymorph. The 2θ range is from 34° to 38° where the main reflection (112) of LCP-*Cmcm* is observed; (**b**) Temperature range from 550 to 800 °C in the 2θ range from 20° to 24°. The transition from the *Pnma* to the $Pn2_1a$ modification is evident from the disappearance of the *Pnma* (101) and (210) reflections and the emergence of the $Pn2_1a$ (210) reflection.

In addition, the morphology of the samples obtained from the ex situ annealing experiments on LCP-*Cmcm* (PO) was examined using SEM (Figure 7). The studies reveal that the nanosheet-like primary structure of the dumbbells continuously changes upon heating. After annealing at 400 °C (Figure 7c), the material starts to sinter and, finally, a denser and more compact material is formed. Simultaneously, the dumbbell-like shape is preserved (Figure 7d,e). At about 700 °C (Figure 7f), the phase transition of the material takes place and the dumbbells start to conglomerate. Further heating (Figure 7g,h) destroys the primary particle shape and results in irregular particles.

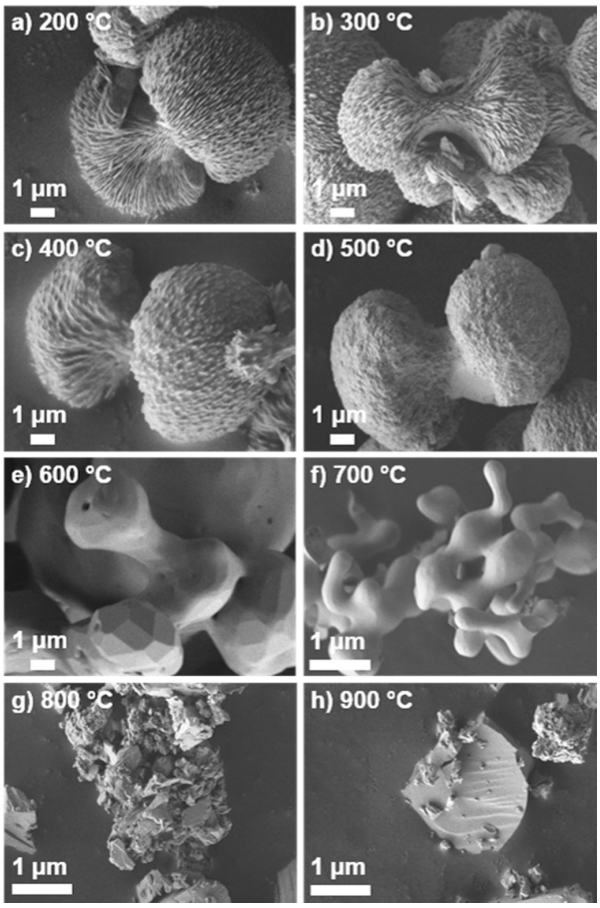


**Figure 7.** SEM images (**a**–**h**) of LCP-*Cmcm* (PO) after annealing in the temperature range from 200 to 900 °C (increment: 100 °C). The samples (**f**–**h**) are shown with higher resolution for clarity.

### *2.5. Magnetic Properties*

The results of the static magnetic susceptibility as a function of the temperature measured on the LCP-*Cmcm* sample are shown in Figure 8. In the high temperature regime, the data obey the Curie-Weiss law ($\chi = \chi_0 + (N_A\mu_{eff}^2)/(3k_b(T-\theta_C))$) with $\chi_0$ being the temperature-independent contribution, $\mu_{eff}$ the effective magnetic moment, $N_A$ the Avogadro number, $\theta_C$ the Weiss temperature (negative value), and $k_b$ the Boltzmann constant. Table 2 shows the results of the Curie-Weiss fitting for the measurements at 1, 10 and 25 kOe.

**Table 2.** Results of the Curie-Weiss fitting in the high temperature regime for LCP-*Cmcm* sample produced by polyol method.

| Variable | 1 kOe | 10 kOe | 25 kOe |
|---|---|---|---|
| $T_N$ (K) | 12.7 | 12.7 | 9.1 |
| $\theta_C$ (K) | −27.6 | −27.7 | −26.2 |
| $\chi_0$ (cm$^3$/mol) | $1.35 \times 10^{-1}$ | $1.73 \times 10^{-1}$ | $1.48 \times 10^{-1}$ |
| $\mu_{eff}$ ($\mu_B$) | 5.46 | 5.42 | 5.56 |

In Figure 8, the ZFC curves reveal a long range antiferromagnetic order below the Néel temperature $T_N$, as result of the antiparallel alignment of magnetic moments of cobalt atoms. As seen in Table 2, the values of the magnetic moments are slightly higher in comparison to the ones reported for high spin octahedral cobalt (II) complexes (4.7 to 5.2 $\mu_B$) [38]. As reported for LCP-*Pnma*, the large value of the effective magnetic moment can be explained by the strongly coupled Co–O–Co superexchange

interactions with $Co^{2+}$ magnetic moments or higher order interactions, such as, Co–O–P–O–Co [39,40]. On the other hand, the behavior of zero-field-cooled (ZFC) and field-cooled (FC) curves below the Néel temperature changes with the increasing magnetic field. At 1 kOe (Figure 8a) the ZFC–FC curves are overlapping, then at 10 kOe (Figure 8b), below the Néel temperature, the FC curve presents susceptibility values that are slightly higher in comparison with the ZFC data. Finally, at 25 kOe, the ZFC–FC curves present a branch point suggesting a magnetic transition depending of the temperature and magnitude of the external magnetic field. This behavior can be confirmed by the magnetization measurements. The isothermal measurements of the magnetization as a function of the applied field are shown in Figure 9. At room temperature (green line), the sample exhibits a paramagnetic behavior. However, when the temperature decreases to values near to $T_N$ (11 K), the sample presents a slightly double hysteresis behavior (blue line) which is increased when the temperature reaches 2 K (black line). The magnetic field-induced phase transition occurs at about 10 kOe caused by the switching from an antiferromagnetic to ferro (or ferri) magnetic state upon increasing the magnetic field. In literature, a weak-ferromagnetic to an antiferromagnetic state transition in LCP-*Pnma* was reported [41], caused by a distortion of the octahedral, formed by cobalt and oxygen atoms at low temperatures ($T$ = 23 K); however, in order to study the origin of these metamagnetic transitions as well as the magnetic structure in different magnetic states, neutron powder diffraction experiments are required for LCP-*Cmcm*.

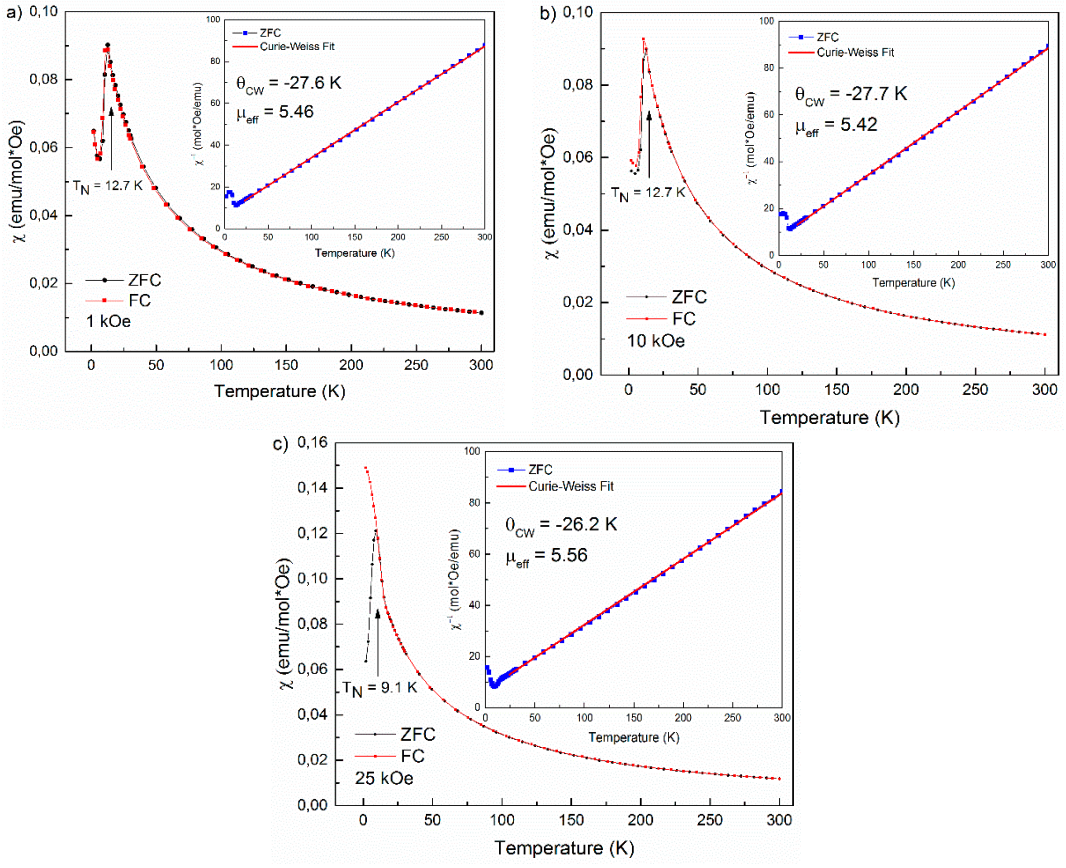


**Figure 8.** Magnetic susceptibility as a function of the temperature at zero-field-cooled/field-cooled (ZFC/FC) conditions under constant applied fields of: (**a**) 1 kOe; (**b**) 10 kOe; and (**c**) 25 kOe for LCP-*Cmcm* produced by polyol method. The inset shows the inverse magnetic susceptibility and the Curie-Weiss fitting of the high temperature data under ZFC conditions.

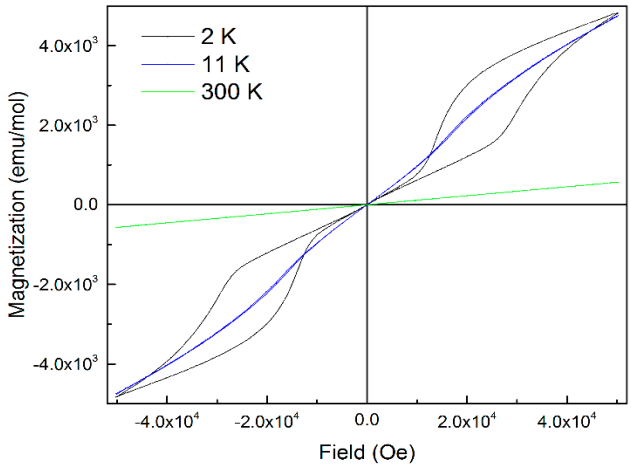


**Figure 9.** Magnetization as a function of the applied field between 5 and −5 T measured at 2, 11 and 300 K for the sample of LCP-*Cmcm* (PO).

## 3. Materials and Methods

### *3.1. Solvothermal Synthesis*

For the solvothermal synthesis of LCP-*Cmcm*, stoichiometric amounts of $CoC_2O_4{\cdot}2H_2O$ (Alfa Aesar, Ward Hill, MA, USA, 98%) and $LiH_2PO_4$ (Sigma Aldrich, St. Louis, MO, USA, 99%) were introduced in 9 mL of solvent, whereas diethylene glycol (DEG; Merck, Darmstadt, Germany, ≥99.0%), triethylene glycol (TEG; Merck, ≥99%), and tetraethylene glycol (TTEG; Merck, ≥98%) were used. The resulting suspensions were homogenized for 20 min, transferred to Teflon-lined stainless steel pressure vessels (BERGHOF Products + Instruments GmbH, Eningen, Germany), and sealed. For the solvothermal treatment, the temperature was ramped to 220 °C within 2 h. After a reaction period of 7 days, the mixtures were cooled to ambient temperature. The resulting bright pink precipitates were separated by suction filtration, washed several times with distilled water (Millipore water type I, 18.2 MΩ·cm) and absolute ethanol (VWR BDH PROLABO AnalaR NORMAPUR, Radnor, PA, USA, 99.95%) followed by drying in air at 130 °C overnight.

### *3.2. Polyol Synthesis*

Powder samples were prepared via a polyol process using cobalt acetate tetrahydrate ($Co(CH_3COO)_2{\cdot}4H_2O$, Merck, 99.99%), lithium acetate ($Li(CH_3COO)$, ChemPUR, Karlsruhe, Germany, 99+%) and $H_3PO_4$ (Merck, 85%) in a stoichiometric molar ratio of 1:3:10. Tetraethylene glycol (TTEG, Merck, ≥99.0%) was used as solvent. First, lithium acetate was solved in 125 mL of TTEG and, subsequently, phosphoric acid added dropwise. Cobalt acetate was dissolved in 75 mL of TTEG and then added to the prior solution. The mixture was refluxed at 200 °C for 14 h in a three-necked round bottom flask. After cooling down to room temperature, the precipitate was separated from the solvent by centrifugation (1500 rpm, 20 min) and washed several times with ethanol (VWR AnalaR NORMAPUR, 99.95%) in order to remove the solvent. The light pink powder was collected by suction filtration, washed with acetone (99% VWR, Semi grade), and dried in air at 120 °C overnight. The material obtained from the polyol process is denoted as LCP-*Cmcm* (PO).

### *3.3. Structural, Physical and Chemical Properties Determination*

X-ray powder diffraction data were collected at room temperature on a STADI P diffractometer (STOE & Cie. GmbH, Darmstadt, Germany) using Mo Kα radiation (Ge(111) monochromator, λ = 0.70930 Å) equipped with a Mythen DCS 1K silicon solid-state detector (Dectris Ltd., Baden-Daettwil, Switzerland). The ground samples were sealed in glass capillaries (Hilgenberg,

Malsfeld, Germany, borosilicate glass type no. 50, length: 80 mm, diameter: 0.5 mm, wall thickness: 0.01 mm), which were then measured in a 2θ range of 3°–60° (PSD (position sensitive detector) step: 0.15°; time/step: 30 s, three ranges, total measurement time: 12 h). An external calibration was performed using Si ($a$ = 5.43088 Å, NBS standard reference material). The JANA2006 software [42] was used for Rietveld analysis of the diffraction patterns. The structure data of the LNP polymorph (ICSD database no. 97767 [20]) were taken as a starting model and refined in the space group C*mcm*.

The temperature-dependent XRD studies were done in situ with a Stoe STADI P diffractometer using Cu Kα radiation (Ge(111) monochromator, λ = 1.540598 Å) equipped with a Dectris Mythen 1K OEM (Dectris Ltd.) silicon solid-state detector. The data were collected between 19° and 37.93° 2θ. The detailed temperature program is provided in Table S5 in the Supplementary Materials.

High-resolution scanning electron microscopy (HR-SEM) was performed on a JSM-7500F instrument (JEOL, Tokyo, Japan) at an accelerating voltage of 1 kV. The powders were prepared on carbon tape, which was attached to an aluminum stub.

Elemental analysis of the sample was carried out by atomic absorption spectroscopy using a Varian AA280FS sequential device for the lithium and cobalt, and by photometry using a UV-160 device (Shimadzu, Kyoto, Japan) for the P contents. CHNS analysis was performed by combustion analysis using a Euro EA CHNSO Analyzer (HEKAtech, Wegberg, Germany).

Attenuated total reflectance (ATR)-FTIR data were collected on a 670 IR FTIR spectrometer (Varian, Palo Alto, CA, USA) equipped with a PIKE GladiATR ATR stage (400–4000 $cm^{-1}$, 132 scans) (see Supplementary Materials). The Resolution Pro software (Agilent, Santa Clara, CA, USA) was used for data handling.

The thermal analysis was carried out to assess the chemical stability of the powders up to 900 °C on a TGA/DSC 1 STAR system (Mettler Toledo, Columbus, OH, USA). Experiments were run at a heating rate of 10 °C·$min^{-1}$ in an argon stream flowing at 10 mL·$min^{-1}$ (specimen weight of 20 mg). The effect of the thermal treatment as a function of temperature was additionally examined using ex situ powder XRD studies (Mo Kα radiation (Ge(111) monochromator, λ = 0.70930 Å, 2θ range of 5°–50°, PSD step: 0.49°; time/step: 10 s, two ranges). For this purpose, approximately 50 mg of the sample were annealed for 6 h in air at temperatures ranging from 200 to 900 °C with an increment of 100 °C using a muffle furnace.

DC magnetization data were collected using a MPMS XL5 superconducting quantum interference device (SQUID, Quantum Design, San Diego, CA, USA). The temperature-dependent data were obtained by measurement of the magnetization from 1.8 to 300 K in an applied magnetic field of 1, 10 and 25 kOe, by using the powdered samples fixed in calibrated gelatin capsules held at the center of a drinking straw. The temperature-dependent measurements were performed in zero-field-cooled (ZFC) and field-cooled (FC) mode. Magnetization as a function of applied field measurements were done between 5 and −5 T at 2, 11 K, and room temperature.

## 4. Conclusions

$LiCoPO_4$-*Cmcm* was synthesized by two different kinetically controlled synthesis approaches. Whereas the product of the solvothermal process showed secondary phases of $Li_3PO_4$ and the olivine-type *Pnma* phase, the polyol process results in the formation of a single-phase LCP-*Cmcm* material in a one-step synthesis without post-annealing. Using the polyol method, a dumbbell-like morphology could be obtained by a simple one-step synthesis without the use of additional surfactants or templates. Moreover, by a simple methodology based on the variation of the mixing order of the educts, the morphology of the samples can be controlled. The temperature-dependent in situ powder X-ray diffraction (PXRD) analysis reveals the phase transitions between the three reported LCP polymorphs. Starting from the *Cmcm* phase, a transition to the *Pnma* structure is observed at 575 °C, which then converts to the $Pn2_1a$ polymorph at 675 °C. After cooling to ambient temperature, the thermodynamically stable *Pnma* modification is obtained. At temperatures above 675 °C, the $Pn2_1a$ polymorph is thermodynamically stable in contrast to that reported at room temperature. To the best

of our knowledge, this behavior is reported for the first time. Moreover, also the hitherto unknown magnetic properties of the *Cmcm* phase were investigated. The LCP-*Cmcm* polymorph shows an antiferromagnetic order below the Néel temperature at low fields (1 and 10 kOe) The measurements of the magnetic response confirm a transition from antiferromagnetic ordering to ferromagnetic (or ferrimagnetic) ordering at temperatures below $T_N$ as a function of the applied field. This study paves the way for a novel methodology towards the synthesis and investigation of new polymorphs of transition-metal phosphates. Thus, our approach provides insights into studying potential cathode materials for lithium-ion batteries from a fundamental point of view.

**Supplementary Materials:** The following are available online at www.mdpi.com/2304-6740/4/4/35/s1. Rietveld refinement details, infrared spectra, PXRD pattern of the sample obtained after the temperature-dependent in situ PXRD measurement, temperature program for temperature-dependent PXRD measurements. Further details of the crystal structure investigation may be obtained from FIZ Karlsruhe, 76344 Eggenstein-Leopoldshafen, Germany (Fax: +49-7247-808-666; E-mail: crysdata@fiz-karlsruhe.de), on quoting the deposition numbers CSD 432183–432186.

**Acknowledgments:** The authors would like to thank the BMW AG, the DAAD, Colciencias, and the Fonds der Chemischen Industrie for financial support and the state of Bavaria and the TUM for X-Ray powder diffractometer funding. Furthermore, we thank Dr. Wilhelm Klein for the in situ XRD measurements, Katia Rodewald for SEM, Gergana Nenova for SQUID, and Pankaj Madkikar for thermogravimetric measurements. We further thank the microanalytical laboratory of the TUM for elemental analyses. Carlos Alarcón-Suesca and Jennifer Ludwig are further grateful to the DAAD, Fonds der Chemischen Industrie for their fellowships.

**Author Contributions:** The manuscript was written through contributions of Carlos Alarcón-Suesca, Jennifer Ludwig, Viktor Hlukhyy, Christoph Stinner and Tom Nilges. Carlos Alarcón-Suesca and Jennifer Ludwig contributed equally to this study.

**Conflicts of Interest:** The authors declare no conflict of interest.

## References

1. Whittingham, M.S. Electrical energy storage and intercalation chemistry. *Science* **1976**, *192*, 1126–1127. [CrossRef] [PubMed]
2. Thackeray, M. Lithium-ion batteries: An unexpected conductor. *Nat. Mater.* **2002**, *1*, 81–82. [CrossRef] [PubMed]
3. Tarascon, J.M.; Armand, M. Issues and challenges facing rechargeable lithium batteries. *Nature* **2001**, *414*, 359–367. [CrossRef] [PubMed]
4. Xu, B.; Qian, D.; Wang, Z.; Meng, Y.S. Recent progress in cathode materials research for advanced lithium ion batteries. *Mater. Sci. Eng. R Rep.* **2012**, *73*, 51–65. [CrossRef]
5. Padhi, A.K.; Nanjundaswamy, K.S.; Goodenough, J.B. Phospho-olivines as positive-electrode materials for rechargeable lithium batteries. *J. Electrochem. Soc.* **1997**, *144*, 1188–1194. [CrossRef]
6. Hautier, G.; Jain, A.; Ong, S.P.; Kang, B.; Moore, C.; Doe, R.; Ceder, G. Phosphates as lithium-ion battery cathodes: An evaluation based on high-throughput ab initio calculations. *Chem. Mater.* **2011**, *23*, 3495–3508. [CrossRef]
7. Strobridge, F.C.; Clement, R.J.; Leskes, M.; Middlemiss, D.S.; Borkiewicz, O.J.; Wiaderek, K.M.; Chapman, K.W.; Chupas, P.J.; Grey, C.P. Identifying the structure of the intermediate, $Li_{2/3}CoPO_4$, formed during electrochemical cycling of $LiCoPO_4$. *Chem. Mater.* **2014**, *26*, 6193–6205. [CrossRef] [PubMed]
8. Sergio, B.; Stefania, P. Recent Advances in the Development of $LiCoPO_4$ as High Voltage Cathode Material for Li-Ion Batteries. In *Nanotechnology for Sustainable Energy*; American Chemical Society: Washington, DC, USA, 2013; Volume 1140, pp. 67–99.
9. Howard, W.F.; Spotnitz, R.M. Theoretical evaluation of high-energy lithium metal phosphate cathode materials in Li-ion batteries. *J. Power Sources* **2007**, *165*, 887–891. [CrossRef]
10. Wolfenstine, J.; Allen, J.L.; Jow, T.R.; Thompson, T.; Sakamoto, J.; Jo, H.; Choe, H. $LiCoPO_4$ mechanical properties evaluated by nanoindentation. *Ceram. Int.* **2014**, *40*, 13673–13677. [CrossRef]
11. Chen, H.; Chen, M.; Du, C.; Cui, Y.; Zuo, P.; Cheng, X.; Yin, G. Synthesis and electrochemical performance of hierarchical nanocomposite of carbon coated $LiCoPO_4$ crosslinked by graphene. *Mater. Chem. Phys.* **2016**, *171*, 6–10. [CrossRef]

12. Theil, S.; Fleischhammer, M.; Axmann, P.; Wohlfahrt-Mehrens, M. Experimental investigations on the electrochemical and thermal behaviour of $LiCoPO_4$-based cathode. *J. Power Sources* **2013**, *222*, 72–78. [CrossRef]
13. Yamada, A.; Hosoya, M.; Chung, S.-C.; Kudo, Y.; Hinokuma, K.; Liu, K.-Y.; Nishi, Y. Olivine-type cathodes: Achievements and problems. *J. Power Sources* **2003**, *119–121*, 232–238. [CrossRef]
14. Ellis, B.L.; Lee, K.T.; Nazar, L.F. Positive electrode materials for Li-ion and Li-batteries. *Chem. Mater.* **2010**, *22*, 691–714. [CrossRef]
15. Truong, Q.D.; Devaraju, M.K.; Ganbe, Y.; Tomai, T.; Honma, I. Controlling the shape of $LiCoPO_4$ nanocrystals by supercritical fluid process for enhanced energy storage properties. *Sci. Rep.* **2014**, *4*. [CrossRef] [PubMed]
16. Morgan, D.; van der Ven, A.; Ceder, G. Li conductivity in $Li_xMPO_4$ (M = Mn, Fe, Co, Ni) olivine materials. *Electrochem. Solid State Lett.* **2004**, *7*, A30–A32. [CrossRef]
17. Tealdi, C.; Spreafico, C.; Mustarelli, P. Lithium diffusion in $Li_{1-x}FePO_4$: The effect of cationic disorder. *J. Mater. Chem.* **2012**, *22*, 24870–24876. [CrossRef]
18. Jaehne, C.; Neef, C.; Koo, C.; Meyer, H.-P.; Klingeler, R. A new $LiCoPO_4$ polymorph via low temperature synthesis. *J. Mater. Chem. A* **2013**, *1*, 2856–2862. [CrossRef]
19. Amador, U.; Gallardo-Amores, J.M.; Heymann, G.; Huppertz, H.; Moran, E.; Arroyo, Y.D.D.M.E. High pressure polymorphs of $LiCoPO_4$ and $LiCoAsO_4$. *Solid State Sci.* **2009**, *11*, 343–348. [CrossRef]
20. Garcia-Moreno, O.; Alvarez-Vega, M.; Garcia-Alvarado, F.; Garcia-Jaca, J.; Gallardo-Amores, J.M.; Sanjuan, M.L.; Amador, U. Influence of the structure on the electrochemical performance of lithium transition metal phosphates as cathodic materials in rechargeable lithium batteries: A new high-pressure form of $Li_xMPO_4$ (M = Fe and Ni). *Chem. Mater.* **2001**, *13*, 2455. [CrossRef]
21. Kreder, K.J.; Assat, G.; Manthiram, A. Microwave-assisted solvothermal synthesis of three polymorphs of $LiCoPO_4$ and their electrochemical properties. *Chem. Mater.* **2015**, *27*, 5543–5549. [CrossRef]
22. Assat, G.; Manthiram, A. Rapid microwave-assisted solvothermal synthesis of non-olivine *Cmcm* polymorphs of $LiMPO_4$ (M = Mn, Fe, Co, and Ni) at low temperature and pressure. *Inorg. Chem.* **2015**, *54*, 10015–10022. [CrossRef] [PubMed]
23. Wang, F.; Zhao, M.; Song, X. Influence of the preparation conditions on the morphology and electrochemical performance of nano-sized Cu–Sn alloy anodes. *J. Alloy. Compd.* **2007**, *439*, 249–253. [CrossRef]
24. Pan, Q.; Jin, H.; Wang, H.; Yin, G. Flower-like cuo film-electrode for lithium ion batteries and the effect of surface morphology on electrochemical performance. *Electrochim. Acta* **2007**, *53*, 951–956. [CrossRef]
25. Tang, K.; Sun, J.; Yu, X.; Li, H.; Huang, X. Electrochemical performance of $LiFePO_4$ thin films with different morphology and crystallinity. *Electrochim. Acta* **2009**, *54*, 6565–6569. [CrossRef]
26. Dinh, H.-C.; Mho, S.-I.; Yeo, I.-H. Electrochemical analysis of conductive polymer-coated $LiFePO_4$ nanocrystalline cathodes with controlled morphology. *Electroanalysis* **2011**, *23*, 2079–2086. [CrossRef]
27. Ryu, W.-H.; Lim, S.-J.; Kim, W.-K.; Kwon, H. 3-D dumbbell-like $LiNi_{1/3}Mn_{1/3}Co_{1/3}O_2$ cathode materials assembled with nano-building blocks for lithium-ion batteries. *J. Power Sources* **2014**, *257*, 186–191. [CrossRef]
28. Zhou, N.; Uchaker, E.; Wang, H.-Y.; Zhang, M.; Liu, S.-Q.; Liu, Y.-N.; Wu, X.; Cao, G.; Li, H. Additive-free solvothermal synthesis of hierarchical flower-like $LiFePO_4$/C mesocrystal and its electrochemical performance. *RSC Adv.* **2013**, *3*, 19366–19374. [CrossRef]
29. Cao, J.; Zhu, Y.; Bao, K.; Shi, L.; Liu, S.; Qian, Y. Microscale $Mn_2O_3$ hollow structures: Sphere, cube, ellipsoid, dumbbell, and their phenol adsorption properties. *J. Phys. Chem. C* **2009**, *113*, 17755–17760. [CrossRef]
30. Zeng, G.; Caputo, R.; Carriazo, D.; Luo, L.; Niederberger, M. Tailoring two polymorphs of $LiFePO_4$ by efficient microwave-assisted synthesis: A combined experimental and theoretical study. *Chem. Mater.* **2013**, *25*, 3399–3407. [CrossRef]
31. Eftekhari, A. Surface modification of thin-film based $LiCoPO_4$ 5 V cathode with metal oxide. *J. Electrochem. Soc.* **2004**, *151*, A1456–A1460. [CrossRef]
32. Choi, D.; Li, X.; Henderson, W.A.; Huang, Q.; Nune, S.K.; Lemmon, J.P.; Sprenkle, V.L. $LiCoPO_4$ cathode from a $CoHPO_4 \cdot xH_2O$ nanoplate precursor for high voltage Li-ion batteries. *Heliyon* **2016**, *2*, e00081. [CrossRef] [PubMed]
33. Ludwig, J.; Marino, C.; Haering, D.; Stinner, C.; Nordlund, D.; Doeff, M.M.; Gasteiger, H.A.; Nilges, T. Facile, ethylene glycol-promoted microwave-assisted solvothermal synthesis of high-performance $LiCoPO_4$ as a high-voltage cathode material for lithium-ion batteries. *RSC Adv.* **2016**, *6*, 82984–82994. [CrossRef]

34. Yang, H.; Wu, X.-L.; Cao, M.-H.; Guo, Y.-G. Solvothermal synthesis of $LiFePO_4$ hierarchically dumbbell-like microstructures by nanoplate self-assembly and their application as a cathode material in lithium-ion batteries. *J. Phys. Chem. C* **2009**, *113*, 3345–3351. [CrossRef]
35. Mathew, V.; Alfaruqi, M.H.; Gim, J.; Song, J.; Kim, S.; Ahn, D.; Kim, J. Morphology-controlled $LiFePO_4$ cathodes by a simple polyol reaction for Li-ion batteries. *Mater. Charact.* **2014**, *89*, 93–101. [CrossRef]
36. Ni, J.; Wang, H.; Gao, L.; Lu, L. A high-performance $LiCoPO_4$/C core/shell composite for Li-ion batteries. *Electrochim. Acta* **2012**, *70*, 349–354. [CrossRef]
37. Huang, X.; Ma, J.; Wu, P.; Hu, Y.; Dai, J.; Zhu, Z.; Chen, H.; Wang, H. Hydrothermal synthesis of $LiCoPO_4$ cathode materials for rechargeable lithium ion batteries. *Mater. Lett.* **2005**, *59*, 578–582. [CrossRef]
38. Nicholls, D. 41-Cobalt. In *The Chemistry of Iron, Cobalt and Nickel*; Pergamon Press: Oxford, UK, 1973; pp. 1053–1107.
39. Szewczyk, A.; Gutowska, M.U.; Wieckowski, J.; Wisniewski, A.; Puzniak, R.; Diduszko, R.; Kharchenko, Y.; Kharchenko, M.F.; Schmid, H. Phase transitions in single-crystalline magnetoelectric $LiCoPO_4$. *Phys. Rev. B* **2011**, *84*, 104419. [CrossRef]
40. Tian, W.; Li, J.; Lynn, J.W.; Zarestky, J.L.; Vaknin, D. Spin dynamics in the magnetoelectric effect compound $LiCoPO_4$. *Phys. Rev. B* **2008**, *78*, 6. [CrossRef]
41. Rhee, C.H.; Kim, S.J.; Kim, C.S. Crystallographic and magnetic properties of $LiCoPO_4$ at low temperature. *J. Korean Phys. Soc.* **2010**, *56*, 611–614.
42. Petricek, V.; Dusek, M.; Palatinus, L. Crystallographic computing system Jana2006: General features. *Z. Kristallogr.* **2014**, *229*, 345–352.
43. Finger, L.W.; Cox, D.E.; Jephcoat, A.P. A correction for powder diffraction peak asymmetry due to axial divergence. *J. Appl. Crystallogr.* **1994**, *27*, 892–900. [CrossRef]
44. Cromer, D.T.; Liberman, D.A. Anomalous dispersion calculations near to and on the long-wavelength side of an absorption edge. *Acta Crystallogr. Sect. A* **1981**, *A37*, 267–268. [CrossRef]
45. Berar, J.F.; Lelann, P. E.S.D.'s and estimated probable error obtained in rietveld refinements with local correlations. *J. Appl. Crystallogr.* **1991**, *24*, 1–5. [CrossRef]
46. Steger, E.; Herzog, K. Zum schwingungsspektrum der phosphorsäure. I. Infrarot- und raman-spektren von phosphatlösungen. *Z. Anorg. Allg. Chem.* **1964**, *331*, 169–182. [CrossRef]
47. Jastrzębski, W.; Sitarz, M.; Rokita, M.; Bułat, K. Infrared spectroscopy of different phosphates structures. *Spectrochim. Acta A Mol. Biomol. Spectrosc.* **2011**, *79*, 722–727. [CrossRef] [PubMed]
48. Poovizhi, P.N.; Selladurai, S. Study of pristine and carbon-coated $LiCoPO_4$ olivine material synthesized by modified sol-gel method. *Ionics* **2011**, *17*, 13–19. [CrossRef]
49. Burba, C.M.; Frech, R. Vibrational spectroscopic investigation of structurally-related $LiFePO_4$, $NaFePO_4$, and $FePO_4$ compounds. *Spectrochim. Acta A Mol. Biomol. Spectrosc.* **2006**, *65*, 44–50. [CrossRef] [PubMed]